Structure of Pseudomonas aeruginosa ribosomes from an aminoglycoside-resistant clinical isolate

Halfon, Yehuda; Jimenez-Fernandez, Alicia; La Rosa, Ruggero; Espinosa Portero, Rocio; Krogh Johansen, Helle; Matzov, Donna; Eyal, Zohar; Bashan, Anat; Zimmerman, Ella; Belousoff, Matthew; Molin, Søren; Yonath, Ada

Published in:
Proceedings of the National Academy of Sciences of the United States of America

DOI:
10.1073/pnas.1909831116

Publication date:
2019

Document version
Publisher's PDF, also known as Version of record

Structure of *Pseudomonas aeruginosa* ribosomes from an aminoglycoside-resistant clinical isolate

Yehuda Halfon[a,1], Alicia Jimenez-Fernandez[b,1,2], Ruggero La Rosa[b], Rocio Espinosa Portero[b,3], Helle Krogh Johansen[c,d], Donna Matzov[a], Zohar Eyal[a], Anat Bashan[a], Ella Zimmerman[a], Matthew Belousoff[e], Søren Molin[b,4], and Ada Yonath[a,4]

[a]Department of Structural Biology, The Weizmann Institute of Science, 7610001 Rehovot, Israel; [b]The Novo Nordisk Foundation Center for Biosustainability, Technical University of Denmark, 2800 Kgs. Lyngby, Denmark; [c]Department of Clinical Microbiology, Rigshospitalet, 2100 Copenhagen, Denmark; [d]Department of Clinical Medicine, Faculty of Health and Medical Sciences, University of Copenhagen, 1165 Copenhagen, Denmark; and [e]Biomedicine Discovery Institute, Department of Microbiology, Monash University, 3800 Clayton, VIC, Australia

Contributed by Ada Yonath, September 4, 2019 (sent for review June 10, 2019; reviewed by Alexander S. Mankin and Huang Ziwei)

Resistance to antibiotics has become a major threat to modern medicine. The ribosome plays a fundamental role in cell vitality by the translation of the genetic code into proteins; hence, it is a major target for clinically useful antibiotics. We report here the cryo-electron microscopy structures of the ribosome of a pathogenic aminoglycoside (AG)-resistant *Pseudomonas aeruginosa* strain, as well as of a nonresistance strain isolated from a cystic fibrosis patient. The structural studies disclosed defective ribosome complex formation due to a conformational change of rRNA helix H69, an essential intersubunit bridge, and a secondary binding site of the AGs. In addition, a stable conformation of nucleotides A1486 and A1487, pointing into helix h44, is created compared to a non-AG-bound ribosome. We suggest that altering the conformations of ribosomal protein uL6 and rRNA helix H69, which interact with initiation-factor IF2, interferes with proper protein synthesis initiation.

ribosome | antibiotic | resistance | aminoglycoside | cystic fibrosis

Aminoglycosides (AGs), which are frequently used for the treatment of many Gram-negative and some Gram-positive infections, are also routinely applied against *Pseudomonas aeruginosa* (PA) infections in cystic fibrosis (CF) patients (1, 2). These antibiotics bind to bacterial ribosomes and inhibit transfer RNA's (tRNA's) translocation, reduce translational fidelity, modify the ribosome subunits' mobility, inhibit ribosome recycling (3), interfere with formation of the intersubunit bridges, and consequentially prevent protein synthesis (4–7). This is achieved by primary binding to helix 44 (h44) of the 16S ribosomal RNA (rRNA), displacing nucleotides A1492 and A1493 (A1486 and A1487 in PA numbering) in the 30S subunit (8, 9). Additional elements within the AG binding pocket include the universally conserved protein uS12, G522 of h18 (G530 in *Escherichia coli* numbering), and A1903 of large subunit (LSU) H69 (A1913 in *E. coli*). The secondary AG binding site to helix 69 (H69) of the 23S rRNA in the 50S subunit may also play a role in AG-mediated protein synthesis inhibition (6, 10).

Resistance to AGs is mainly acquired by 3 mechanisms: 1) reduced uptake of the drugs due to decreased permeability of the cell membrane and overexpression of efflux pumps, which actively expel the drugs (11); 2) acquisition of AG-modifying enzymes, encoded by mobile genetic elements, which chemically modify and inactivate the drug (12); and 3) by 16S rRNA methyltransferases (RMTases), which methylate specific nucleotides in the antibiotic binding site of the 16S rRNA, preventing binding of the antibiotic (N7-G1405 16S-RMTases and N1-A1408 16S-RMTases) (13, 14). In general, antibiotic resistance is often caused by mutations at or near the drug binding site (15). Therefore, antibiotic treatment of infections is expected to result in an accumulation of mutations in genes encoding rRNAs and ribosomal proteins (rProteins). However, such mutations are not commonly observed in clinically isolated strains, and only a limited number have been identified in *E. coli* and *Mycobacterium tuberculosis* (15–18). One explanation for this apparent absence of such target mutations could be that mutations in ribosomal genes may result in decreased within-host fitness when the selective pressure is removed. Additionally, resistance mutations in rRNA genes need to be recombined into all copies of the chromosomal rRNA genes before full antibiotic resistance is developed.

Recently, in a large collection of whole-genome-sequenced clinical PA isolates from early stage lung infections in CF patients (19), we identified 2 strains infecting the same patient (358 and 359). These 2 isolates had minimum inhibitory concentration (MIC) values for the AG tobramycin that were 128-fold (358) and 8-fold (359) higher than the European Committee on Antimicrobial Susceptibility Testing clinical breakpoint for this

Significance

The cryo-electron microscopy high-resolution structures of the wild-type ribosome of the human pathogen *Pseudomonas aeruginosa* and its uL6 rProtein mutant, isolated from a cystic fibrosis (CF) patient, shed light on the link between a distorted initiation factor 2 (IF2) binding site, a deletion in uL6, and a 50-Å distal H69–h44 B2a&b intersubunit bridges. These cumulative structural alterations interfere with the initiation of proper protein synthesis. Here, via efforts at understanding a specific and so-far-unknown aminoglycoside (AG)-resistant mechanism, we widen the concept of diversity of resistance mechanisms. Thus, we reveal a defective ribosome obtained by a conformational change of essential ribosomal intersubunit bridges and an alteration of the secondary AG binding site.

Author contributions: Y.H., A.J.-F., A.B., E.Z., S.M., and A.Y. designed research; Y.H., A.J.-F., R.E.P., D.M., Z.E., E.Z., and M.B. performed research; H.K.J. contributed new reagents/analytic tools; Y.H., A.J.-F., R.L.R., R.E.P., A.B., and S.M. analyzed data; and Y.H., A.J.-F., R.L.R., A.B., S.M., and A.Y. wrote the paper.

Reviewers: A.S.M., University of Illinois at Chicago; and H.Z., School of Medicine, University of California San Diego.

The authors declare no competing interest.

Data deposition: Atomic coordinates and EM maps for the reported EM structures have been deposited in the Protein Data Bank, https://www.rcsb.org/ (PDB ID codes 6SPG, 6SPD, 6SPE, 6SPF, 6SPB, and 6SPC) and the Electron Microscopy Data Bank, https://www.ebi.ac.uk/pdbe/emdb/ (accession nos. 10285, 10282, 10283, 10284, 10280, and 1028), respectively.

[1]Y.H. and A.J.-F. contributed equally to this work.

[2]Present address: Department of Plant Microbe Interaction, Max Planck Institute for Plant Breeding Research, D-50829 Cologne, Germany.

[3]Present address: Department of Biomolecular Sciences, University of Copenhagen, 1165 Copenhagen, Denmark.

[4]To whom correspondence may be addressed. Email: sm@bio.dtu.dk or ada.yonath@weizmann.ac.il.

This article contains supporting information online at www.pnas.org/lookup/suppl/doi:10.1073/pnas.1909831116/-/DCSupplemental.

First published October 14, 2019.

antibiotic. The values for gentamicin were 128-fold (358) and 16-fold (359) higher (MIC assessed by Etest at the clinic). Searching for mutations potentially involved in AG resistance in the 2 strains (358 and 359) revealed an in-frame 12-nucleotide deletion (-GCTTTGTAACCA) in the *rplF* ribosomal gene, encoding the uL6 protein of the 50S subunit, in both isolates, which were not identified in any other isolate from this collection. The mutation results in a GYKA deletion after amino acid residue 92 and a resulting shorter loop of the C-terminal domain of the uL6 rProtein, which could be the cause of the observed phenotype.

Here, we report the structure of the ribosome from the PA 358 clinical strain harboring the 12-nucleotide deletion in the *rplF* gene and the structure of the ribosome from the wild-type iso-clonal isolate (366), carrying a nonmutated *rplF*. In order to shed light on the phenotypic behavior, high-resolution cryo-electron microscopy (cryo-EM) structures of ribosomes from both the wild-type and the mutant ribosomes were determined and comparatively analyzed. Based on our results, we propose an explanation for the formation of defective ribosome complex and a weak AG binder. A conformational change of H69 and a shorter uL6 loop may interfere with proper binding of initiation factor 2 (IF2) and, hence, with proper protein synthesis initiation.

Results

The rplF Mutation Causes a Reduction in Growth Rate and Resistance to Gentamicin. The generation times of isolates 359 and 358 were of 1 h and 40 min on average, 2.6- ± 0.1-fold higher than those of the native isolates (366 and 368) that only required 40 min to double their population in our growth conditions. Since both clinical uL6 mutant strains showed a reduced growth rate and an increased AG resistance relative to the native strains, we evaluated the effect of the mutation on both phenotypes by complementation analysis of the strains. Plasmid-mediated complementation of the *rplF* mutation by expressing a wild-type copy of the *rplF* gene under its own promoter showed a statistically significant increase in growth rate (68% relative to mutant strain containing the pCE [empty] vector plasmid; Student's *t* test; $P < 0.0001$) (Fig. 1*A*) and a considerable decrease in MIC to gentamicin (Fig. 1*B*), indicating a direct relationship between growth rate and ribosome functionality.

Determining the gentamicin susceptibility in vitro (half-maximal inhibitory concentration [IC_{50}]), using a cell-free coupled transcription–translation system, showed a 1.8- and 2.3-fold higher IC_{50} (1-way ANOVA followed by Tukey's post hoc test; $P < 0.001$) for the mutant strain relative to the native strain and to PAO1 wild-type ATCC strains, respectively (Fig. 1*C*). These results agree with the determined MIC for gentamicin of the respective clinical strains.

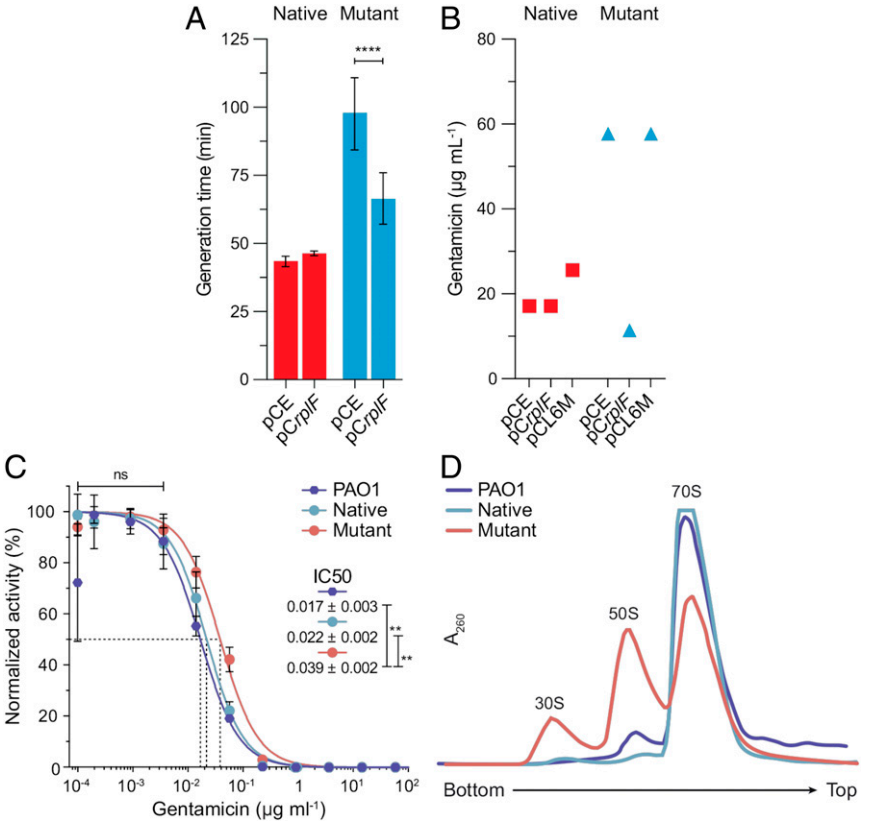

Fig. 1. Effect of *rplF* mutation on growth phenotype and gentamicin resistance. (*A*) Complementation assay of *rplf* mutation. The wild-type copy of *rplF* gene was expressed from a plasmid (pC*rplF*) in native and mutant strains and the generation time was assessed. The empty plasmid (pCE) was used as control. Error bars represent the SD of 3 independent replicates. Differences between conditions were computed by using the student test ($P < 0.0001$). (*B*) MIC for gentamicin antibiotic for the native and mutant strains containing the pCE empty plasmid, the pC*rplF* plasmid containing the wild-type copy of the *rplF* gene, and the pCL6M plasmid containing the mutated copy of the *rplF* gene. (*C*) Inhibition of translation as results of increasing concentrations of gentamicin antibiotic resulting from the translation of the firefly luciferase in vitro translation system. Note that at low gentamicin concentrations (1×10^{-4} to 3.6×10^{-3} µg·mL^{-1}), the in vitro translational activity is comparable between wild-type (PAO1 and native) and mutant ribosomes. ns, not significant differences. The values represent the mean ± SE ($n = 3$) of the luminescence. Differences between the IC_{50} values were computed by using 1-way ANOVA followed by Tukey's post hoc test ($P < 0.01$). (*D*) Molecular assessment of the ribosome functionality. Sedimentation profiles (10–50% sucrose gradient) of wild-type (PAO1 and native) and *rplF* mutant total ribosome fraction are shown.

The uL6 Deletion Reduces the Fraction of Translationally Active Ribosomes. In bacteria, the content of active ribosomes determines growth rate (20). Since the *rplF* mutant strains showed reduced growth rates compared with wild-type strains, we analyzed the consequences of the uL6 mutation for the structure and function of the mutant ribosomes. Sucrose gradient analysis of the ribosomal particles from native and mutant strains revealed that *uL6 mutant* ribosomes are characterized by reduced 70S particle fractions relative to separated 30S and 50S free subunits (Fig. 1*D*). Since translational activity depends on assembled 70S particles, the suggested in vivo instability of the uL6 mutant ribosomes may explain the reduced growth rates of the mutant strains.

Cryo-EM Near-Atomic Structures of Native and uL6 Mutant PA Ribosomes. To further investigate the resistance mechanism and growth defects of the uL6 mutated ribosomes, we employed single-particle cryo-EM techniques. We determined and compared the structures of intact ribosomes purified from the native (PAnat) and the uL6 mutant (PAuL6m) clinical isolates (Fig. 2*A*). The nominal map resolutions for 70S ribosomes were 3.3 and 2.9 Å and for the 50S subunits 3.3 and 2.8 Å, respectively (*SI Appendix*, Figs. S1 and S2). Importantly, the resolution of the maps extended to 2.2 Å in the core regions, enabling us to build and refine an atomic model for both the ancestor and the mutant (*SI Appendix*, Table S1).

Unique Features of the PA Ribosomes. Comparing the structure of PAnat ribosome to other known ribosome structures revealed certain unique PA ribosome structural features. We highlight structural differences in rRNA H45 and H16 (Fig. 2 *B* and *C*), where these helices are the shortest for PAnat; and rRNA H63 (Fig. 2*D*), where this helix is longer in PAnat and *E. coli* ribosomes. In the small subunit, 2 unique sites were identified in rRNA helixes. In h7 (Fig. 2*E*), the ribosomes of the 3 pathogens exhibited a longer helix than in *Thermus thermophilus*. In

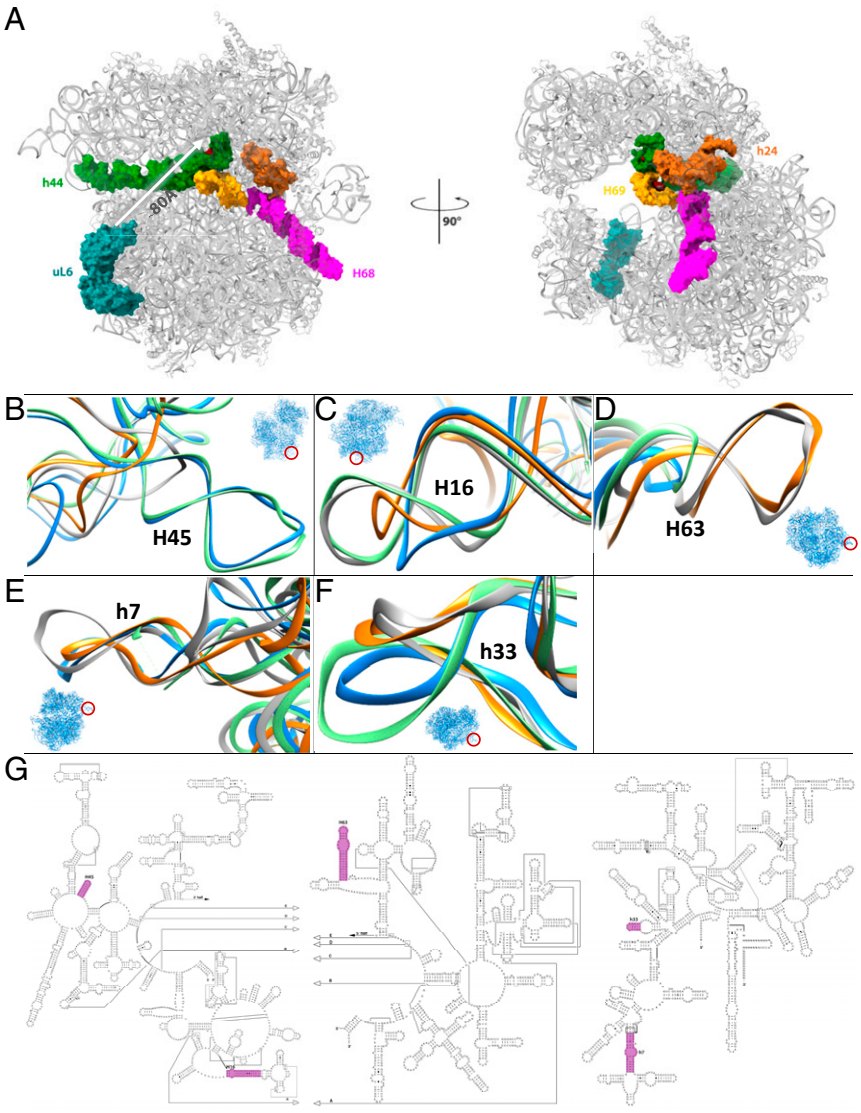

Fig. 2. (*A*) The cryo-EM structure of the PA ribosome where uL6, H69, H68, h44, h24, and paromomycin are shown as space-filling objects and are colored blue, yellow, magenta, green, orange, and red, respectively. The PA ribosome is shown in 2 views 90° apart. (*B–F*) Structure comparison between PAnat, *E. coli*, *S. aureus*, and *T. thermophilus*. (*B*) Large subunit rRNA helix H45. (*C*) Large subunit rRNA helix H16. (*D*) Large subunit rRNA helix H63. (*E*) Small subunit rRNA helix h7. (*F*) Small subunit rRNA helix h33. PA, *E. coli* (PDB ID code 5NWY), *S. aureus* (PDB ID code 5TV7), and *T. thermophilus* (PDB ID code 5IMQ) are shown in orange, gray, blue, and green, respectively. (*G*) The location of the rRNA helices shown in *B–F* is marked on the 2D map of the PA ribosome.

contrast, h33 (Fig. 2*F*) of *T. thermophilus* is the longest and widest helix compared to those of the 3 pathogenic ones, whereas in *E. coli* and PAnat, they are the shortest. Targeting such specific rRNA sites (Fig. 2*G*) may be effective against PA and mutant strains, which are resistant to the common drugs used against PA such as tobramycin and gentamicin.

Structural Comparison of Both PAnat and PAuL6m Mutant Ribosomes. The comparison between the ribosome structures reveals important differences. First, wild-type rProtein uL6 shows a longer loop in the PAnat ribosome than the mutant PAuL6m protein, due to the deletion, which is clearly seen in the maps (Fig. 3*A* and *SI Appendix*, Fig. S3). Second, the 2 universally conserved nucleotides A1486 and A1487 (*E. coli* A1492 and A1493) in the PAnat structure are facing outward from the AG binding site, while in PAuL6m, the nucleotides face inward (Fig. 3*B*). Furthermore, H69 of the PAuL6m is bent toward the large subunit compared to the intersubunit bridge that is formed between the 2 subunits in the PAnat ribosome (Fig. 3*C* and *SI Appendix*, Fig. S4). H69 is located in close proximity to the AG main binding site, and its bending may diminish these interactions, which may explain at least part of the resistance phenotype of the mutant strain. An additional intersubunit bridge that is formed between H68 and h24 in the PAnat ribosome structure is not visible in the structure of PAuL6m (Fig. 3*D*).

Discussion

The growth defects of the PA mutant can be attributed to the disruption of the formation of the B2a and B2b intersubunit bridges. H69 is part of the intersubunit bridge B2a, one of the main bridges that stabilize the 70S ribosome, connecting the decoding and the peptidyl transferase center sites. H69 of the PAuL6m ribosome is bent in such a way that the correct intersubunit bridge cannot be formed. h24 is part of the small subunit and part of the intersubunit bridge B2b. It forms the bridge with H68 of the large subunit. In the PAnat ribosome, the bridge could be traced and modeled. However, h24 could not be traced in the maps of PAuL6m, due to lack of density, which hints at the intersubunit bridge destabilization. These findings are in accord with the sucrose-gradient determinations of the ribosomal subunit ratio, 70S particles vs. 30S + 50S subunits, showing that lower amounts of translationally active 70S ribosomes were harvested from the uL6 mutant strain in comparison to ribosomes isolated from the PA native strain, which may explain why the mutant bacteria grow slower than the native strain. Moreover, H69 is located in close proximity to the AG main binding site, and its bending diminishes the formation of a confined binding site. In addition, the 2 universally conserved nucleotides A1486 and A1487 (*E. coli* A1492 and A1493), which face inward from h44 in PAuL6m, may lead to a weaker AG binding, since effective binding requires their rotation.

Accurate tRNA selection by the ribosome is essential for the synthesis of functional proteins. Previous structural studies have indicated that the ribosome distinguishes between cognate and near-cognate tRNAs by monitoring the geometry of the codon–anticodon interactions of the universally conserved 16S ribosomal RNA bases G530, A1492, and A1493 in the decoding center (21, 22). During decoding, nucleotides A1492 and A1493 flip out of h44, G530 moves from a *syn* to an *anti* conformation, and each of these 3 bases interacts with the minor groove of the codon–anticodon helix. AG binding at the upper part of h44 (main AG binding site) and subsequent displacement of A1492 and A1493 cause significant miscoding, block intersubunit rotation, and inhibit translocation. The well-defined electron-density map around these nucleotides in the PAuL6m EM map points at their stabilized orientation within h44, which may preclude the AG binding, since effective binding requires outward rotation of

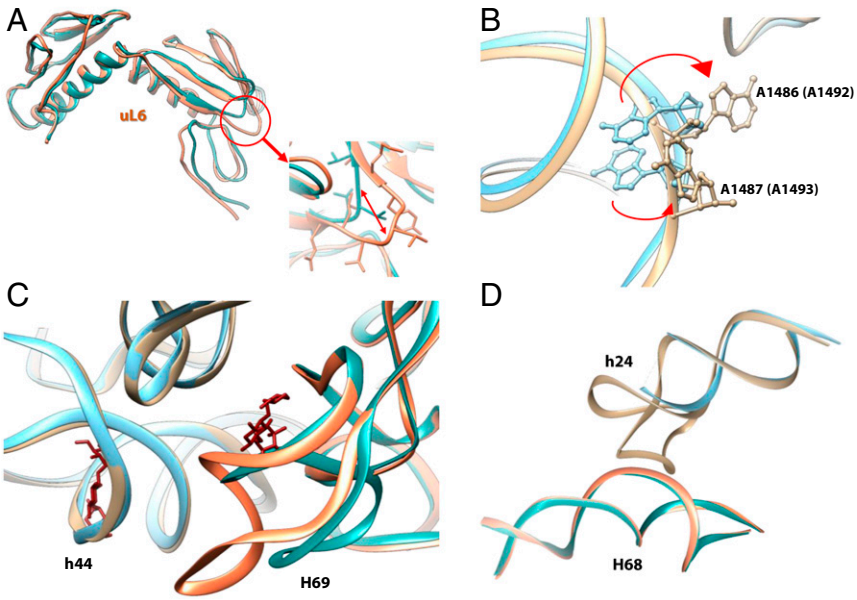

Fig. 3. The specific differences found between the PA native and mutant ribosomes. (*A*) A comparison of the uL6 protein of PAnat (coral) and PAuL6m (cyan). The red arrow marks the structural alteration of the loop due to the GYKA deletion. (*B*) Differences at the structure of the main AG binding site in h44 of the 16S rRNA. The red arrows indicate the flipping of the nucleotides (PA and *E. coli* [in brackets] numbering are used). PAnat and PAuL6m 16S rRNA are shown in tan and blue, respectively. (*C*) Conformational changes of intersubunit bridge B2a: gentamycin (colored in red) is superimposed on its main binding site at h44 and its secondary binding site at H69, from PDB ID code 4V53 (45). H69 (cyan) and h44 (blue) of PAuL6m were superimposed on PAnat helices H69 (wheat) and h44 (orange) to show the conformational changes that occur in H69 that contribute to the phenotypic characteristics of the mutant. It may also harm the binding to the second AG binding site at H69. (*D*) Conformational changes at intersubunit bridge B2b: H68 (cyan) and h24 (blue) of PAuL6m were superimposed on PAnat helices H68 (wheat) and h24 (orange) to show the flexible region of h24 that was not modeled and contribute to the phenotypic characteristics of the mutant.

the 2 nucleotides. Nevertheless, it seems that both structures reflect the known flexibility of the 2 nucleotides, which is needed for their activity (Fig. 3*B*). Hence, this difference is probably not the main reason for the lower sensitivity of the mutant toward AG. The secondary AG binding site is in H69, and a modification in its structure may interfere with binding of AGs to that site (Fig. 3*C*).

We suggest that a distorted IF2 binding is the link between the deletion mutation in the uL6m rProtein and the H69–h44 B2a bridge. IF2 (Fig. 4*A*) is a multidomain initiation factor, which in complex with GTP binds to fMet–tRNA^{fMet} through its domain IV and to the mRNA-associated 30S subunit (23), guiding major structural rearrangements in the ribosome during initiation. Upon GTP hydrolysis, IF2 undergoes large conformational changes, eliminating proper interactions between IF2 and the 70S ribosome that are required for the stabilization of the mRNA–ribosome interactions during initiation. Within the 70S ribosome, IF2 interacts on one side with uL6 via the G domain (Fig. 4*B*) and via its domain IV with H69 (Fig. 4*C*), maintaining a close proximity to the P-site tRNA on the other side. For illustration, we superimposed IF2 and the P-site tRNA from PDB ID code 3JCJ (24) on both PA structures (Fig. 4*A*). Zooming in on both interaction sites, we examined the consequences of the mutation in uL6 via the changes in the AG and H69 binding sites, which may explain the instability of 70S subunits and low protein synthesis activity of the PA mutant strain.

At the interaction site between IF2 (in red) and uL6 (Fig. 4*B*), IF2 can interact with the uL6 92 loop of the PAnat and create a similar interaction to that seen in the *E. coli* 70S–fMet-tRNA$_i^{Met}$–IF2$^{–GDPNP}$ complex (23). Thus, a deletion in the loop of the mutant may weaken this interaction. Importantly, sequence alignment of the uL6 protein from 70 bacterial species, shown partially for PA, *E. coli*, *T. thermophilus*, *Bacillus subtilis*, *Staphylococcus aureus*, and *Deinococcus radiodurans* (Fig. 4*D*), indicates that the loop 91–96 is 100% sequence conserved in bacteria. Therefore, the effect of the 4-amino-acid deletion, along with their high conservation, may hint at their significance for the proper ribosome function. This change may lead to the shift of IF2 toward the uL6 loop or destabilize its binding and displace its other end with its IV domain from H69 and initiator P-site tRNA, reaching to the AG binding site.

The overlay of the IF2 structure on the PAuL6m ribosome suggests that H69 of the PAuL6m may clash with IF2 (Fig. 4*C*) or force it to adopt a different conformation. This movement with the lack of bridge B2a may further explain the low stability of the 70S ribosomes in the mutant. Zooming to the tRNA–IF2–H69 interaction site (Fig. 4*C*) shows that H69 of PAuL6m does not block the P-site tRNA binding site.

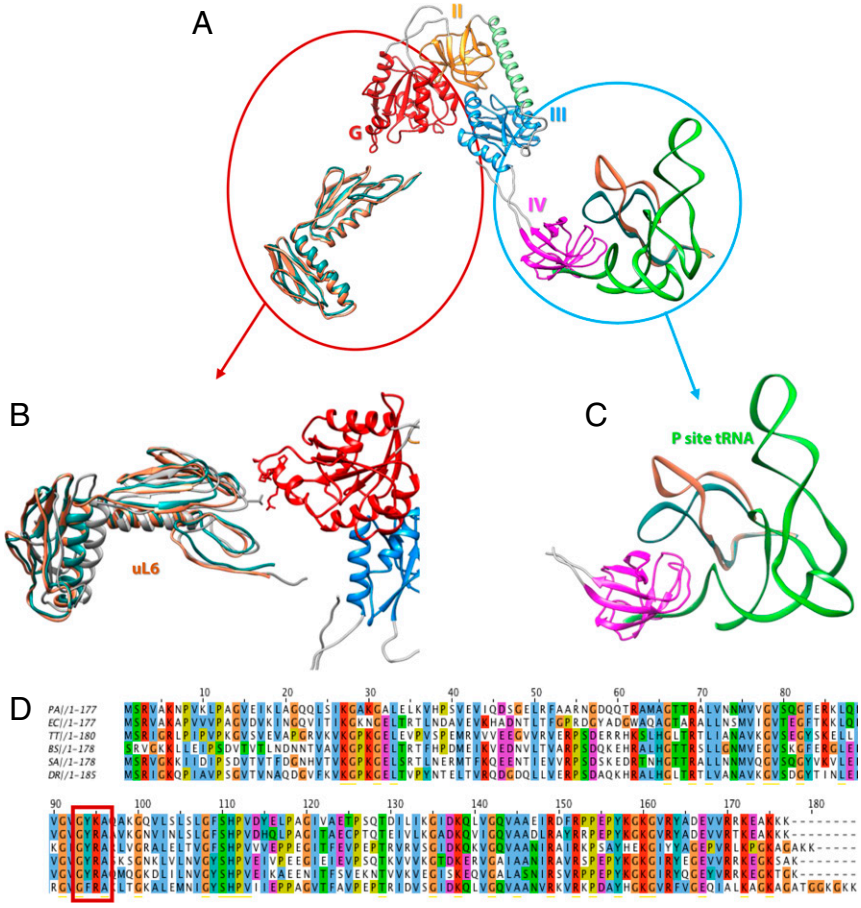

Fig. 4. (*A*) IF2 bridges between uL6 and H69 IF2 (using PDB ID code 3JCJ) superimposed on PAnat (coral) and PAuL6m (cyan) suggests how IF2 is interacting with both uL6 and H69. IF2 domains G, II, III, IV, and h8 are shown in red, orange, blue, purple, and green, respectively. (*B*) Zoom into uL6 from PAnat (coral), PAUL6m (cyan), and *E. coli* (gray) interacting with the IF2 domain G (red). The shorter uL6 loop of PAuL6m (cyan) may hamper this interaction. (*C*) Zoom into H69 superimposed with P-site tRNA (PDB ID code 5LMV) and with the IF2 domain IV (purple). The shift of H69 in PAuL6m mutant toward IF2 domain IV, compared to PAnat, may lead to a clash between IF2 and H69 that may either interfere with IF2 proper binding and may hamper this function of H69. (*D*) Sequence alignment of uL6 protein of PA, *E. coli* (EC), *T. thermophilus* (TT), *B. subtilis* (BS), *S. aureus* (SA), and *D. radiodurans* (DR). The mutation site is marked with a red box.

Interestingly, the AG binding site is located 50 Å distant from the uL6 protein, suggesting that antibiotic resistance can also be acquired by altering the complex structure of the ribosome, affecting its interaction with central auxiliary proteins and that the mechanistic understanding of changes in the overall ribosomal structure may play a key role in mitigating antibiotic resistance. A similar bacterial antibiotic-resistance mechanism, which is based on ribosome splitting and recycling, ensuring efficient translation even in presence of lincomycin and erythromycin, 2 antibiotics that block protein synthesis, has been recently described (25).

Through a genetic, biochemical, and structural analysis of an AG-resistant mutant of PA, we have shown that a deletion in the uL6 rProtein causes a number of phenotypic changes. In addition to resistance to members of the AG family of antibiotics, the deletion causes ribosomal instability and reduced growth rate. The cryo-EM–based structural analysis of wild-type and mutant ribosomes has offered explanations for the changes of these phenotypes as well as predictions for involvement of translational factors in connection with the phenotypic consequences. This is good news for a continued investigation of other ribosomal variant strains obtained from antibiotic-treated CF patients (19).

Materials and Methods

Bacterial Strains and Media. PA clinical isolates were sampled and identified from sputum samples of patient P76M4 attending the Copenhagen Cystic Fibrosis Center at Rigshospitalet, Copenhagen (19). Analyses of the bacterial isolates were approved by the local ethics committee of the Capital Region of Denmark (Region Hovedstaden; registration no. H-4-2015-FSP).

For complementation purposes, rplF under its own promoter was amplified with primers EcoRI_rplF_fwd and HindIII_rplF_rev (TATAAAGCTTATGACCTGGGCGTAAATGTG) from PA PAO1 and mutant clinical isolate and cloned into EcoRI–HindIII–pSEVA332 (26) restriction sites, resulting in pCE (empty vector), pCrplf harboring the wild-type copy of rplf gene, and pCL6M harboring the mutant rplf gene from mutant isolate. Plasmid were transferred by triparental mating as described above using pRK2013 as helper plasmid (27). All cloning PCRs were performed with Phusion Hot Start II High-Fidelity DNA Polymerase (Thermo Fisher).

PCR products were purified and cloned in the pSEVA344 plasmid and transferred to receptor strains via tripartite conjugation by using the pRK2013 helper plasmid.

Bacterial growth was recorded by measuring the turbidity at 600 nm of cell cultures in a 250-mL flask at 250 rpm at 37 °C in Luria–Bertani (LB) medium (28). For each strain, 3 independent biological replicates were analyzed.

Antibiotic Susceptibility Tests. MIC for gentamicin was determined in 96-well microplates in LB medium containing decreasing concentrations (2-fold dilution series) of antibiotic. Plates were incubated for 48 h at 37 °C at 150 rpm. For each strain, 3 independent biological replicates were analyzed.

PA Ribosome Purification. PA cells were grown in LB at 37 °C until mid-exponential phase (0.6–0.8 A_{600}), harvested at 8,000 × *g* for 10 min at 4 °C, and washed twice in buffer A (50 mM Tris·HCl, pH 7.6, 10 mM $MgCl_2$, 100 mM NH_4Cl, 0.5 mM EDTA, pH 8, and 6 mM β-mercaptoethanol). Cellular lysis was carried out as reported (23) in buffer A containing 10 mg/mL lysozyme by freeze–thaw in liquid nitrogen. The lysate was centrifuged at 22,000 rpm for 30 min at 2 °C, and the supernatant was stored at −80 °C. Cell extracts were layered on a 1.1 M sucrose cushion (10 mM Hepes, pH 8.0, 14 mM $MgCl_2$, 100 mM NH_4Cl, 50 mM KCl, and 6 mM β-mercaptoethanol) and ultracentrifuged at 55,000 rpm using a Ti-70 rotor at 4 °C for 17 h. The supernatant was then discarded, and the pellet was dissolved in 50 mM KCl, 14 mM $MgCl_2$, 10 mM Hepes (pH 7.6), 100 mM NH_4Cl, and 6 mM β-mercaptoethanol buffer (pH 8.0) at 4 °C. The 70S ribosomes were purified by sucrose gradient ultracentrifugation, using a SW-28 rotor with a gradient of 10–50% sucrose, at high Mg^{2+} concentration (14 mM $MgCl_2$) for 17.5 h at 18,000 rpm. After separation, the Mg^{2+}concentration was adjusted to 10 mM, and the ribosomes were concentrated by using centrifugation at 32,000 × *g* for 19 h at 4 °C and then further concentrated at 45,000 × *g* for 1.5 h at 4 °C. The samples were kept in 15 mM KCl, 10 mM $MgCl_2$, 10 mM Hepes (pH 7.6), and 60 mM NH_4Cl at pH 7.6, brought to a final concentration not exceeding 1,000 $A_{260}\cdot mL^{-1}$, and then flash-frozen for storage at −80 °C.

In Vitro Inhibition of Translation Assay. The inhibition effect of gentamicin and chloramphenicol on PA ribosomes was tested in a bacterial coupled transcription/translation assay system, where the activity of the firefly luciferase was used as a reporter (29) The luciferase gene was present on a plasmid with T7 RNA polymerase promoter. The inhibition assay, similar to what has been described in ref. 30, was performed in solution containing 160 mM Hepes–KOH (pH 7.5); 6.5% polyethylene glycol 8 K; 0.074 mg/mL tyrosine; 1.3 mM ATP; 0.86 mM CTP, GTP, and UTP; 208 mM potassium glutamate; 83 mM creatine phosphate; 28 mM NH_4OAc; 0.663 mM cyclic adenosine monophosphate, 1.8 mM dithiothreitol, 0.036 mg/mL folinic acid, 0.174 mg/mL *E. coli* tRNA mix, 1 mM amino acid, 8 μM $Mg(OAc)_2$, 0.25 mg/mL creatine kinase, 0.027 mg/mL T7 RNA polymerase, 0.003 μg/μL luciferase plasmid, and *E. coli* S100 lysate (which doesn't include ribosomes) and added 300 nM ribosomes. A concentration range of gentamicin was 2.3 mg/mL to 0.01 ng/mL in 1:2 serial dilutions. The results were plotted, and IC_{50} values were calculated by using the program GraFit (Version 7). IC_{50} values were determined by fitting the inhibition data to a 4-parameter IC_{50} equation: $\frac{range}{1+\left(\frac{x}{IC50}\right)^s}$ where *range* is the maximum *y* range, and *s* is a slope factor. The *x* axis represents the concentration of the analyte. Data fitted to this equation are usually displayed with a logarithmically scaled *x* axis. The visualization of the data were obtained by using GraFit software (31).

Cryo-EM Data Acquisition. Similar to what was described in ref. 32, a volume of 3.5 μL of ribosome samples was applied on glow-discharged holey carbon grids (Quantifoil R1.2/1.3, 200 mesh) on pure ice. The grids were blotted and plunge-frozen by using a Vitrobot Mark IV (FEI Company). Cryo-EM micrographs were recorded at liquid nitrogen temperature on a Titan Krios electron microscope (FEI) operating at 300 kV. Micrographs of PAnat were recorded on a Falcon 2 (FEI) at a magnification of 127,000, pixel size of 1.1 $Å\cdot px^{-1}$, defocus range of 0.5–2.1 μm, and total dose of 42 $e/Å^2$. This dataset was collected at Monash University, Clayton, Australia.

Micrographs of PAuL6m were recorded on a Falcon 3 (FEI) at a magnification of 127,000, pixel size of 1.1 $Å\cdot px^{-1}$, defocus range of 0.5–1.5 μm and total dose of 40 $e/Å^2$. This dataset was collected at the Netherlands Centre for Electron Nanoscopy (NeCEN; Leiden, The Netherlands).

Cryo-EM Image Processing and 3D Reconstructions. Cryo-EM images were subjected to motion correction by using MotionCor2 (33). Contrast transfer function parameters for each micrograph were determined by CTFFIND4 (34). Particle selection, 2D and 3D classifications were performed in RELION (Version 2.1) (35). The resulting particle projections were subjected to further refinement with alignment focusing on the small subunit (SSU) and LSU, respectively. Reported resolutions are based on the gold-standard Fourier shell correlation using the 0.143 criteria (*SI Appendix*, Figs. S1 and S2). Local resolution was determined by using ResMap (36) with half-reconstructions as input maps (*SI Appendix*, Figs. S1 and S2).

Model Building and Refinement. Model building of the ribosomal LSU and SSU was performed by fitting the reported model of the ribosome from *T. thermophilus* (PDB ID code 4LF4) to the calculated density map using Chimera (37). The docked model was manually manipulated by using COOT (38) real-space and geometry-restraint commands to fit into the density maps. De novo sequence-guided model building was applied to additional features that were better resolved in the current maps. The rRNA and protein sequences used for modeling were extracted from the PA whole-genome sequence. Model refinement was performed by a combination of PHENIX (39) and COOT as described (40). Structure validation was done by using Molprobity (41). Model overfitting was evaluated through its refinement against cryo-EM half maps (*SI Appendix*, Fig. S2). Figures were created by using the UCSF Chimera package (37). Local resolution plots were generated in ResMap (36).

Figure Generation and Sequence Alignment. All figures were generated with Chimera and ChimeraX (37, 42). uL6 multiple-sequence alignment was performed by ClustalW (43) and presented by Jalview (44).

ACKNOWLEDGMENTS. We thank the A.Y. and S.M. groups for their interest and experimental support; and Christoph Diebolde for EM data acquisition at NeCEN and helpful advice. This work was supported by European Research Council Grant 322581 (Novel Insights into Multi-Drug Resistance to Antibiotics and the Primordial Ribosome); the Kimmelman Center for Macromolecular Assemblies; Danish Council for Independent Research Grant Rammebevilling DFF-4181-00115; and the Novo Nordisk Foundation. This work was also supported by iNEXT: Infrastructure for NMR, EM and X-Rays for Translational Research Project 653706, funded by the European Union Horizon 2020 program. A.Y. holds the Martin S. and Helen Kimmel Professorial Chair at the Weizmann Institute of Science. A.J.-F. was a recipient of a H.C. Ørsted COFUND Postdoc Fellowship from the Technical University of Denmark.

1. D. N. Wilson, Ribosome-targeting antibiotics and mechanisms of bacterial resistance. *Nat. Rev. Microbiol.* **12**, 35–48 (2014).
2. J. Lin, D. Zhou, T. A. Steitz, Y. S. Polikanov, M. G. Gagnon, Ribosome-targeting antibiotics: Modes of action, mechanisms of resistance, and implications for drug design. *Annu. Rev. Biochem.* **87**, 451–478 (2018).
3. G. Hirokawa *et al*., Post-termination complex disassembly by ribosome recycling factor, a functional tRNA mimic. *EMBO J.* **21**, 2272–2281 (2002).
4. M. V. Rodnina, W. Wintermeyer, Fidelity of aminoacyl-tRNA selection on the ribosome: Kinetic and structural mechanisms. *Annu. Rev. Biochem.* **70**, 415–435 (2001).
5. J. M. Ogle, V. Ramakrishnan, Structural insights into translational fidelity. *Annu. Rev. Biochem.* **74**, 129–177 (2005).
6. M. R. Wasserman *et al*., Chemically related 4,5-linked aminoglycoside antibiotics drive subunit rotation in opposite directions. *Nat. Commun.* **6**, 7896 (2015).
7. S. Garneau-Tsodikova, K. J. Labby, Mechanisms of resistance to aminoglycoside antibiotics: Overview and perspectives. *MedChemComm* **7**, 11–27 (2016).
8. D. Moazed, H. F. Noller, Interaction of antibiotics with functional sites in 16S ribosomal RNA. *Nature* **327**, 389–394 (1987).
9. M. I. Recht, S. Douthwaite, J. D. Puglisi, Basis for prokaryotic specificity of action of aminoglycoside antibiotics. *EMBO J.* **18**, 3133–3138 (1999).
10. L. Wang *et al*., Allosteric control of the ribosome by small-molecule antibiotics. *Nat. Struct. Mol. Biol.* **19**, 957–963 (2012).
11. X. Z. Li, P. Plésiat, H. Nikaido, The challenge of efflux-mediated antibiotic resistance in Gram-negative bacteria. *Clin. Microbiol. Rev.* **28**, 337–418 (2015).
12. M. S. Ramirez, M. E. Tolmasky, Aminoglycoside modifying enzymes. *Drug Resist. Updat.* **13**, 151–171 (2010).
13. J. Wachino, Y. Arakawa, Exogenously acquired 16S rRNA methyltransferases found in aminoglycoside-resistant pathogenic gram-negative bacteria: An update. *Drug Resist. Updat.* **15**, 133–148 (2012).
14. N. Ban *et al*., A new system for naming ribosomal proteins. *Curr. Opin. Struct. Biol.* **24**, 165–169 (2014).
15. J. M. Munita, C. A. Arias, Mechanisms of antibiotic resistance. *Microbiol. Spectr.*, 10.1128/microbiolspec.VMBF-0016-2015 (2016).
16. P. Buckel, A. Buchberger, A. Böck, H. G. Wittmann, Alteration of ribosomal protein L6 in mutants of *Escherichia coli* resistant to gentamicin. *Mol. Gen. Genet.* **158**, 47–54 (1977).
17. R. Kühberger, W. Piepersberg, A. Petzet, P. Buckel, A. Böck, Alteration of ribosomal protein L6 in gentamicin-resistant strains of *Escherichia coli*. Effects on fidelity of protein synthesis. *Biochemistry* **18**, 187–193 (1979).
18. D. Sharma, A. R. Cukras, E. J. Rogers, D. R. Southworth, R. Green, Mutational analysis of S12 protein and implications for the accuracy of decoding by the ribosome. *J. Mol. Biol.* **374**, 1065–1076 (2007).
19. R. L. Marvig, L. M. Sommer, S. Molin, H. K. Johansen, Convergent evolution and adaptation of *Pseudomonas aeruginosa* within patients with cystic fibrosis. *Nat. Genet.* **47**, 57–64 (2015).
20. M. Scott, S. Klumpp, E. M. Mateescu, T. Hwa, Emergence of robust growth laws from optimal regulation of ribosome synthesis. *Mol. Syst. Biol.* **10**, 747 (2014).
21. J. M. Ogle *et al*., Recognition of cognate transfer RNA by the 30S ribosomal subunit. *Science* **292**, 897–902 (2001).
22. N. Demeshkina, L. Jenner, E. Westhof, M. Yusupov, G. Yusupova, A new understanding of the decoding principle on the ribosome. *Nature* **484**, 256–259 (2012).
23. P. Julián *et al*., The cryo-EM structure of a complete 30S translation initiation complex from *Escherichia coli*. *PLoS Biol.* **9**, e1001095 (2011).
24. T. Sprink *et al*., Structures of ribosome-bound initiation factor 2 reveal the mechanism of subunit association. *Sci. Adv.* **2**, e1501502 (2016).
25. M. Duval *et al*., HflXr, a homolog of a ribosome-splitting factor, mediates antibiotic resistance. *Proc. Natl. Acad. Sci. U.S.A.* **115**, 13359–13364 (2018).
26. R. Silva-Rocha *et al*., The standard European vector architecture (SEVA): A coherent platform for the analysis and deployment of complex prokaryotic phenotypes. *Nucleic Acids Res.* **41**, D666–D675 (2013).
27. M. Kahn *et al*., Plasmid cloning vehicles derived from plasmids ColE1, F, R6K, and RK2. *Methods Enzymol.* **68**, 268–280 (1979).
28. J. Sambrook, E. F. Fritsch, T. Maniatis, *Molecular Cloning: A Laboratory Manual* (Cold Spring Harbor Laboratory Press, Cold Spring Harbor, NY, 1989), pp. 931–957.
29. R. W. Murray, E. P. Melchior, J. C. Hagadorn, K. R. Marotti, *Staphylococcus aureus* cell extract transcription-translation assay: Firefly luciferase reporter system for evaluating protein translation inhibitors. *Antimicrob. Agents Chemother.* **45**, 1900–1904 (2001).
30. Y. Halfon *et al*., Exit tunnel modulation as resistance mechanism of S. aureus erythromycin resistant mutant. *Sci. Rep.* **9**, 11460 (2019).
31. R. J. Leatherbarrow, *GraFit Version 7* (Erithacus Software Ltd., Horley, U.K., 2010).
32. M. Shalev-Benami *et al*., Atomic resolution snapshot of *Leishmania* ribosome inhibition by the aminoglycoside paromomycin. *Nat. Commun.* **8**, 1589 (2017).
33. S. Zheng, E. Palovcak, J.-P. Armache, Y. Cheng, D. Agard, Anisotropic correction of beam-induced motion for improved single-particle electron cryo-microscopy. bioRxiv: 10.1101/061960 (4 July 2016).
34. A. Rohou, N. Grigorieff, CTFFIND4: Fast and accurate defocus estimation from electron micrographs. bioRxiv:10.1101/020917 (13 August 2015).
35. S. H. Scheres, RELION: Implementation of a Bayesian approach to cryo-EM structure determination. *J. Struct. Biol.* **180**, 519–530 (2012).
36. A. Kucukelbir, F. J. Sigworth, H. D. Tagare, Quantifying the local resolution of cryo-EM density maps. *Nat. Methods* **11**, 63–65 (2014).
37. E. F. Pettersen *et al*., UCSF Chimera—A visualization system for exploratory research and analysis. *J. Comput. Chem.* **25**, 1605–1612 (2004).
38. P. Emsley, B. Lohkamp, W. G. Scott, K. Cowtan, Features and development of coot. *Acta Crystallogr. D Biol. Crystallogr.* **66**, 486–501 (2010).
39. P. D. Adams *et al*., PHENIX: A comprehensive Python-based system for macromolecular structure solution. *Acta Crystallogr. D Biol. Crystallogr.* **66**, 213–221 (2010).
40. Z. Eyal *et al*., Structural insights into species-specific features of the ribosome from the pathogen *Staphylococcus aureus*. *Proc. Natl. Acad. Sci. U.S.A.* **112**, E5805–E5814 (2015).
41. V. B. Chen *et al*., MolProbity: All-atom structure validation for macromolecular crystallography. *Acta Crystallogr. D Biol. Crystallogr.* **66**, 12–21 (2010).
42. T. D. Goddard *et al*., UCSF ChimeraX: Meeting modern challenges in visualization and analysis. *Protein Sci.* **27**, 14–25 (2018).
43. M. Goujon *et al*., A new bioinformatics analysis tools framework at EMBL-EBI. *Nucleic Acids Res.* **38**, W695–W699 (2010).
44. A. M. Waterhouse, J. B. Procter, D. M. Martin, M. Clamp, G. J. Barton, Jalview Version 2—A multiple sequence alignment editor and analysis workbench. *Bioinformatics* **25**, 1189–1191 (2009).
45. M. A. Borovinskaya *et al*., Structural basis for aminoglycoside inhibition of bacterial ribosome recycling. *Nat. Struct. Mol. Biol.* **14**, 727–732 (2007).